optica

Direct polarization measurement using a multiplexed Pancharatnam-Berry meta-hologram: supplementary material

XUEQIAN ZHANG,[1,*] SHUMIN YANG,[2] WEISHENG YUE,[3] QUAN XU,[1] CHUNXIU TIAN,[4] XIXIANG ZHANG,[4] ERIC PLUM,[5] SHUANG ZHANG,[6] JIAGUANG HAN,[1,*] AND WEILI ZHANG[1,7,*]

[1]*Center for Terahertz waves and College of Precision Instrument and Optoelectronics Engineering, Tianjin University and the Key Laboratory of Optoelectronics Information and Technology (Ministry of Education), Tianjin 300072, China*
[2]*Shanghai Synchrotron Radiation Facility, Shanghai 201204, China*
[3]*Institute of Optics and Electronics, Chinese Academy of Sciences, P.O. Box 350, Chengdu 610209, China*
[4]*Physical Science and Engineering Division, King Abdullah University of Science and Technology (KAUST), Thuwal 23955-6900, Saudi Arabia*
[5]*Optoelectronics Research Centre and Centre for Photonic Metamaterials, University of Southampton, Highfield, Southampton SO17 1BJ, UK*
[6]*School of Physics and Astronomy, University of Birmingham, Birmingham B15 2TT, UK*
[7]*School of Electrical and Computer Engineering, Oklahoma State University, Stillwater, Oklahoma 74078, USA*
*Corresponding author: alearn1988@tju.edu.cn, jiaghan@tju.edu.cn, weili.zhang@okstate.edu

This document provides supplementary information to "Direct polarization measurements by multiplexed Pancharatnam-Berry meta-hologram," http://dx.doi.org/10.1364/optica.99.099999. © 2019 Optical Society of America

http://dx.doi.org/10.1364/optica.99.099999.s1 [supplementary document doi]

Section 1: Fourier transform method for extracting chiral phase differences

The chiral phase difference $\Delta\varphi$ in Eq. (3) of the main manuscript can be extracted through a Fourier transform. Notice that θ is only in the range of 0 – 360°, which would result a poor resolution in the Fourier domain. This can be resolved by making Eq. (3) continuous by translating and copying $|PD_x(\theta)|^2$ with a period of 360°. By taking the Fourier transform, we get:

$$F\left[\left|PD_x(\theta)\right|^2\right] = \pi\left(r_0^2 + l_0^2\right)\delta(k)$$
$$+ \frac{\pi}{2}l_0 r_0\left[\delta\left(\frac{k}{2}+1\right) + \delta\left(\frac{k}{2}-1\right)\right]e^{-jk\frac{\Delta\varphi}{2}}, \quad \textbf{(S1)}$$

where $\delta(k)$ represents the Dirac delta function and k is the coordinate in the Fourier domain. Here, we do not consider the negative values of k. $\Delta\varphi$ can thus be obtained by calculating the phase of $F[|PD_x(\theta)|^2]$ through selecting $k = 2$ (second order): $\Delta\varphi = -\text{ang}(F[|PD_x(\theta)|^2])|_{k=2}$.

In real cases, the generated images are influenced by the zero-order output, and background noise from the algorithm, fabrication derivations and measurement errors, etc. Determining the chiral phase difference by simply identifying the angles of the maxima of the x-polarized intensity distribution along the ring will therefore result in significant measurement uncertainty. However, the Fourier transform can help extract the phase information locked to 2θ, which is more reliable. Therefore, we applied the Fourier transform method to extract the chiral phase difference in the simulations and experiments.

Section 2: Modified Gerchberg-Saxton algorithm

Unlike previously reported polarization-dependent meta-holograms, where phase distributions of the meta-holograms for different polarizations can be designed separately, here, there is a certain phase relation between the two images [Fig. 1(e)]. Therefore, a modified Gerchberg-Saxton (GS) algorithm is proposed, as illustrated in Fig. S1. The basic procedure is similar to the conventional GS algorithm [S1] that is individually carried out for the two images, but we add a step to make a connection between the phases of the two images. The flow of this algorithm is summarized as:

The algorithm starts with two input images, which are shown in Figs. 3(a) and 3(b). L_0 and R_0 represent the corresponding pre-compensated amplitudes with zero initial phase distributions in the image space, respectively. After fast Fourier transforms,
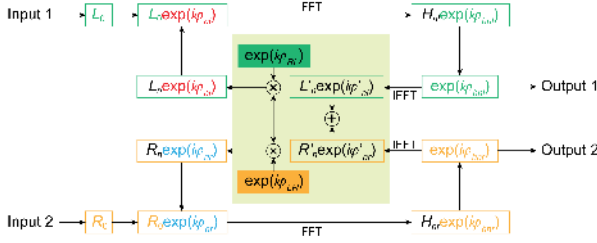
Fig. S1. Flow chart of the modified GS algorithm.

complex amplitude distributions (H_{nl} and H_{nr}) and phase distributions (φ_{hnl} and φ_{hnr}) are separately obtained in the hologram space. To realize phase-only holograms, the amplitude distributions are then replaced with unit amplitude distributions, followed by inverse fast Fourier transforms. L'_n and R'_n are the back-transformed amplitude distributions in the image space, while φ'_{nl} and φ'_{nr} are the corresponding back-transformed phase distributions. Next, the obtained two complex distributions are added together, and separately multiplied with phase terms $\exp(i\varphi_{RL})$ and $\exp(i\varphi_{LR})$, respectively, where $\varphi_{RL} = -\theta$ and $\varphi_{LR} = \theta$ with θ being the azimuth angle. L_n and R_n are the calculated amplitude distributions, while φ_{nl} and φ_{nr} are the corresponding phase distributions, respectively. It should be noted that this step cannot make the final phase distributions of the rings identical to those shown in Figs. 1(c) and 1(d) due to the iteration process, and indeed, this is not necessary. Instead, it guarantees that the phase difference distribution is as shown in Fig. 1(e), and this is sufficient for extraction of the chiral phase difference using the presented method. At last, L_n and R_n are replaced with L_0 and R_0, respectively. The above mentioned procedures formed one loop in the iteration algorithm. The subscript n in the above quantities represents the n-th iteration. After a number of iterations, the final phase distributions for generating these two images are obtained, as illustrated in Figs. 3(c) and 3(d).

Section 3: Mechanism of the twin image generation and simulation confirmation

Here, the Pancharatnam-Berry (PB) phase method is applied to design the meta-hologram. Thus, the phase distribution of the meta-hologram will change its sign under reversed circularly polarized illumination, resulting in generation of a twin image. We multiplexed two meta-holograms, where one (green resonator set) works under left-handed circularly polarized (LCP) illumination, while the other (orange resonator set) works under the right-handed circularly polarized (RCP) illumination. Thus, twin images will always exist. According to the properties of Fourier transforms, the twin image is centrosymmetric and phase conjugate to the designed target image [S2]. Figure S2 schematically illustrates the mechanism of the generation of the target and twin patterns of rings and disks in the proposed meta-hologram, supposing that phase distributions with topological charges of −1 and +1 are assigned to the rings in the target patterns, just as those in Figs. 1(c) and 1(d), respectively. Here, the ring and disk patterns at the left-top corners are the target patterns, while those at the right-bottom corners are the twin patterns. It can be seen from Figs. S2(c) and S2(f) that the twin patterns have identical features with the target patterns, indicating that they can also be applied to measure the polarization state. It should be noted that the assigned phase distributions with topological charges of −1 and +1 are solely for

simple explanation of the mechanism. As long as the phase difference distribution fulfills the design in Fig. 1(e), the metasurface can be used to extract the chiral phase difference according to Eqs. (1) to (3); whereas the phase distributions of the two holographic images do not have to possess the topological charges shown in Figs. 1(c) and 1(d).
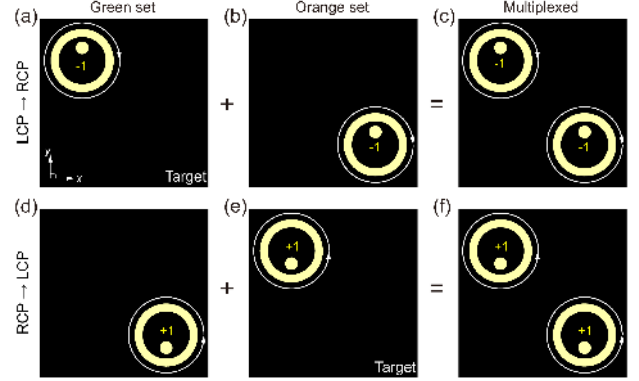

Fig. S2. Schematics of the image generation. (a,e) Schematics of the target RCP and LCP holographic images generated by LCP illumination and RCP illumination of the green and orange resonator sets of the meta-hologram in Fig. 3(f), respectively. (d,b) Schematics of the corresponding LCP and RCP twin images generated by reversed circularly polarized illumination. (c,f) Schematics of the RCP and LCP holographic images generated by LCP illumination and RCP illumination of the multiplexed meta-hologram, respectively.

To confirm the above analysis, we further carry out simulations on the designed meta-hologram to obtain the holographic images, which are done by numerical calculation. First, the amplitude and phase of the transmitted fields of the bar resonators with different orientation angles are extracted in the circular polarization basis. This provides us with the complex transmission coefficients, t_{ll}, t_{lr}, t_{rl}, and t_{rr}, for each bar resonator orientation, where the former subscript represents the output polarization state, the latter subscript represents the input polarization state, l and r represent the LCP and RCP light, respectively. Then, the incident polarization is decomposed into the LCP component E_l and RCP component E_r. At last, the far-field radiation pattern is calculated using the Rayleigh-Sommerfeld diffraction method by considering each bar resonator as a point source of transmitted left-handed field, $t_{ll}E_l$ and $t_{lr}E_r$, and right-handed field, $t_{rr}E_r$ and $t_{rl}E_l$, and regarding the field of the incident wave as uniformly distributed [S3].

Figure S3 illustrates the corresponding simulated normalized amplitude distributions of the RCP and LCP holographic images generated respectively under LCP illumination and RCP illumination, as well as their phase difference distribution. It is seen that the amplitude distributions agree well with those indicated in Fig. S2. In particular, the phase difference distributions along the ring show clear topological charges of −2 in both the target and twin images. These features clearly demonstrate that both the target and twin patterns of the rings and disks in the design can be used to measure the polarization state.
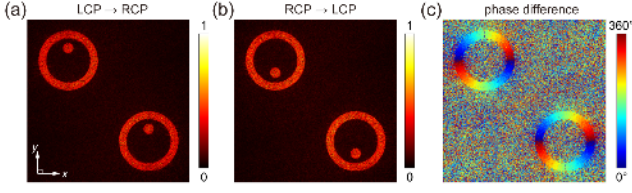
2

Fig. S3. Simulated holographic images. (a,b) Simulated normalized field amplitude distributions of the RCP and LCP holographic images generated by LCP illumination and RCP illumination, respectively. The corresponding intensity distributions are proportional to the square of the amplitude distributions. (c) Simulated phase difference distributions between the holographic images in (a) and (b). The speckles in (a) and (b) are the background noise induced by the modified GS algorithm.

Section 4: Eigen transmittance spectra and resonance modes of the bar resonator

Figure S4(a) shows simulation results of the transmittance spectra of the bar resonator under x- and y-polarized illuminations. There are two eigen resonances in the relevant wavelength range, one at 828 nm along the length (y) of the bar, and the other at 586 nm along the width (x) of the bar. The corresponding simulated resonant field distributions and schematics of the current density distributions are shown in Figs. S4(b) and S4(c). Both of the two resonances are typical dipolar resonances.
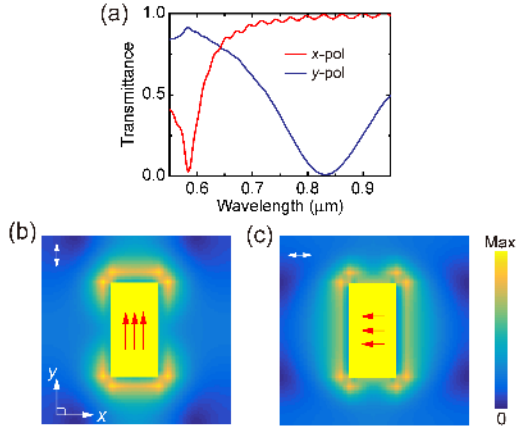

Fig. S4. Transmittance spectra and resonant electric field distributions of a periodic gold bar resonator array at normal incidence. (a) Simulated transmittance spectra under x- and y-polarized illuminations. (b,c) Simulated electric field magnitude $|E|$ in the plane of the bars under (b) y-polarized illumination at 828 nm wavelength and (c) x-polarized illumination at 586 nm wavelength. The red arrows schematically illustrate the corresponding current density distributions.

Section 5: Fabrication process of the proposed meta-hologram

First, layers of 180-nm-thick PMMA (A4, 4000 RPM; 180°C, 90 s) and 40-nm-thick conductive resist (AR-PC5090.02; 90°C, 2 min) were spin-coated on the substrate successively, as illustrated in Figs. S5(a) and S5(b). Then, the pattern of the bar resonators in the meta-hologram was written using electron beam lithography

(CRESTEC, CABL-9500C), as illustrated in Fig. S5(c). After that, the conductive resist was removed using deionized water (2 min), while the exposed PMMA in the bar regions was developed in a solution of MIBK and IPA with 1:3 ratio (45 s) and rinsed in alcohol (30 s), as illustrated in Fig. S5(d). Next, 5 nm of chromium were deposited on top of it as an adhesion layer, followed by 40-nm-thick gold (MANTIS DEPOSITUON LTD, QPrep Deposition System), as illustrated in Fig. S5(e). At last, the metallic film outside the bar regions was removed by a lift-off process in acetone (10 min with ultrasound), as illustrated in Fig. S5(f).
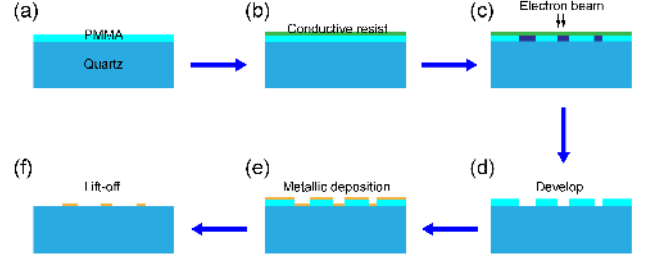

Fig. S5. Flowchart of the meta-hologram fabrication. (a) PMMA coating. (b) Conductive resist coating. (c) Electron beam lithography. (d) Development. (e) Metal deposition. (f) Lift-off.

Section 6: Preliminary measurement

Figure S6(a) schematically illustrates a preliminary projection measurement of the metasurface. A linear polarizer (LP1) was used to initialize the polarization of the 798 nm wavelength continuous wave laser to the x-polarization. A quarter or half wave plate (WP) was then used to control the polarization state of the laser light that was then focused normally onto the metasurface by lens 1. After that, a linear polarizer (LP2) was used to select the x-polarized component of the transmitted light, which was projected onto a screen placed about 30 cm behind the metasurface to reveal the holographic image. The image was recorded using a camera, where an IR viewer was placed before the camera to enhance the signal. Here, only the image that is projected onto the target area [black screen quadrant in Fig. S6(a)] is captured.

Figures S6(b) to S6(e) show the detected x-polarized component of the holographic images generated by LCP, RCP, x-polarized and y-polarized metasurface illuminations, respectively. Clear features of the predicted results are observed. Under LCP illumination and RCP illumination, only rings containing either upper or lower circular disks are generated, respectively. The detected x-polarized intensity distributions along the rings have no obvious regular oscillations. These results verify that our circular-polarization-dependent meta-hologram behaves as intended. Under x-polarized illumination and y-polarized illumination, the intensities of the circular disks are approximately equal, indicating similar strengths of the incident LCP and RCP components with a circular amplitude contrast of about 1. The detected x-polarized intensity distributions along the rings show obvious regular oscillations. The maxima emerge around azimuthal positions of 0° and 180° for x-polarized illumination, indicating a circular phase difference of 0°; while incident y-polarization results in maxima at 90° and 270° corresponding to a circular phase difference of 180°. This behavior agrees well with the theoretical prediction. In particular, this confirms the existence of the intended phase difference distribution along the ring. It should be mentioned

that the higher intensities near the right-bottom corner of the measured images are due to proximity of the zero-order output at the center of the screen. Since the efficiency of the applied single-layer plasmonic metasurface is very low, even the side envelope and the fields scattered by the structures and some impurities of the zero-order output can reach the intensity level of the generated holographic image. This is confirmed by the measurement in Fig. S6(e), where the intensity near the right-bottom corner nearly disappears due to the fact that the zero-order-related outputs are blocked by LP2, which does not transmit the incident *y*-polarization.

With such a configuration, a simple holographic polarimeter can be realized by projecting the holographic image onto a pre-defined dial plate to determine the circular phase difference and two balanced power detectors for measuring the chiral amplitude contrast.
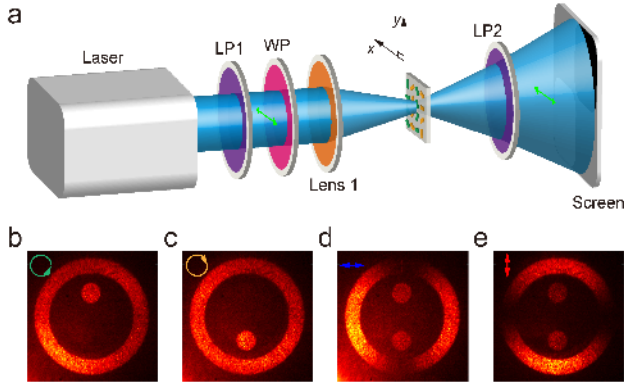

Fig. S6. Preliminary demonstration of holographic polarimetry. (a) Schematic of the experimental setup for the preliminary measurements. LP: linear polarizer; WP: half or quarter wave plate. Green arrows indicate the polarization state after LP1 and LP2. (b)–(e) Holographic images projected onto the black area of the screen under LCP, RCP, *x*-polarized and *y*-polarized metasurface illuminations, respectively. The inset arrows indicate the corresponding incident polarization states generated by the combination of LP1 and WP.

Section 7: Fabrication tolerance of the proposed meta-hologram

In real cases, fabrication errors mainly cause the lengths, widths and orientation angles of the fabricated structures to deviate from the design, leading to additional noise affecting the amplitude and phase distributions of the meta-hologram. Without loss of generality, we add random noise of ±10% to ±40% to the meta-hologram's amplitude, phase and resonator orientation distributions [S4]. Here, the percentage specifies end points of a uniform noise distribution. Amplitude noise is relative noise applied to the designed amplitude of co- and cross-polarized transmission. Phase noise is absolute noise specified as a fraction of the 360° range of possible phase values and is applied to the designed phase of co- and cross-polarized transmission. Orientation angle noise is absolute noise specified as a fraction of the 180° range of possible bar orientations. Figure S7 shows the corresponding simulated results at the design wavelength of 800 nm, in which the amplitude distributions under LCP illumination and RCP illumination are plotted alongside the corresponding phase difference

distributions. It is seen that the dimensions of the ring/disk, as well as the features of the phase difference distributions, are very stable and visible even at ±30% noise level. However, the overall amplitudes of the rings and disks gradually decrease and the holographic images become noiser as the amplitude of the applied noise increases, which will reduce the polarization measurement performance. When the noise level increases to ±40%, the designed holographic features disappear.
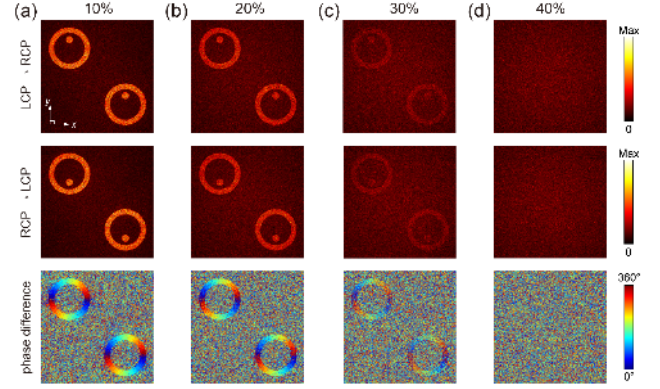

Fig. S7. Fabrication tolerance of the meta-hologram. (a-d) Simulated amplitude distributions of the RCP (upper row) and LCP (middle row) holographic images generated under LCP illumination (upper row) and RCP illumination (middle row), as well as their phase difference distributions (bottom row), with random noise of ±10% (a), ±20% (b), ±30% (c), and ±40% (d) applied to the meta-hologram's amplitude, phase and resonator orientation distributions.

Section 8: Method of extracting the chiral phase difference and the Stokes parameters

Here, we show an example to illustrate the extraction of a polarization state. Figure S8(a) shows the simulated *x*-polarized component of the holographic image generated under *x*-polarized illumination. Here, the *x*-polarized component is obtained by extracting the *x*-polarized component of each simulated far-field holographic image generated by $E_i t_{jk}$ and combining them by complex addition, where $i, j, k \in [l, r]$. Once the holographic image is obtained, we could then extract the polarization state.

First, the intensity distribution along the ring is extracted. To enhance the signal to noise ratio, the intensities in the ring region at each azimuth angle θ are considered, as schematically illustrated by the orange ring region in Fig. S8(a). By integrating the intensity over the ring width (the inset back arrow) at each azimuth angle θ from 0° to 360°, the corresponding intensity distribution along the ring is obtained, as shown by the orange line in Fig. S8(b). It can be seen that there are many oscillations induced by the noise, which makes it hard to read the value of the chiral phase difference directly. [This problem is more serious without integration, if the intensity distribution is just extracted along the blue circle (central line of the ring) in Fig. S8(a), see the blue line in Fig. S8(b).]

Next, a Fourier transform is carried on the extracted integrated intensity distribution (extended to 10 periods). Figure S8(c) shows the amplitude (top) and phase (bottom) of the Fourier transform. The phase value at the 2nd order (indicated by a dash line) equals the opposite of the chiral phase difference, see Section 1.

Then, we integrate the intensities over a certain area of the upper and lower disks [green areas in Fig. S8(a)] as well as an equally large area at the center of the ring [purple area in Fig. S8(a)] for noise subtraction and to determine the chiral amplitude contrast. The corresponding extracted values are shown in Fig. S8(d).

At last, the Stoke parameters of the incident polarization state are calculated from the above values using (4) to (6).
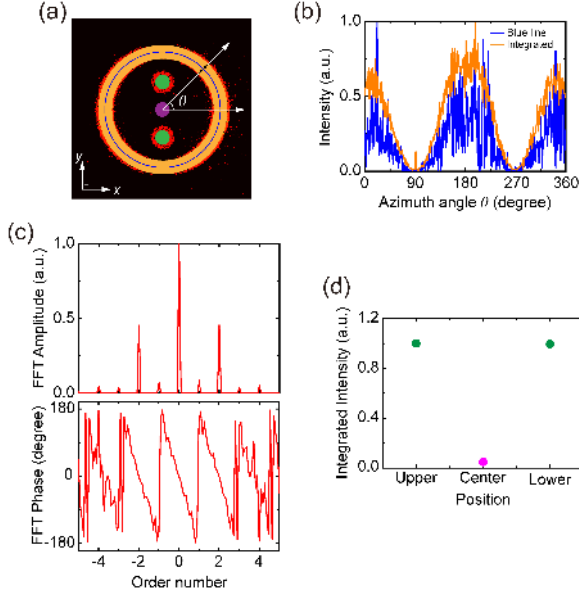

Fig. S8. Characterization of the meta-hologram. (a) Ring (orange), dot (green) and reference (purple) integration areas plotted on the simulated *x*-polarized component of the holographic image (red) generated by *x*-polarized metasurface illumination. (b) Intensity distributions along the ring. Blue: along the central blue line in (a). Orange: integrated over the ring width. (c) Amplitude (top) and phase (bottom) of the Fourier transform of the orange line in (b) extended to 10 periods. (d) Integrated intensities over the green- and purple-shaded disk areas in (a).

Section 9: Broadband characteristics of the proposed metasurface polarimetry

The meta-hologram was designed for a wavelength of 800 nm. When the wavelength of the incident beam deviates from it, the dimension of the holographic image will change. Figures S9(a) to S9(d) show the simulated holographic images generated under LCP illumination at wavelengths of 650, 800, 850 and 900 nm, respectively. It is seen that larger wavelengths correspond to larger image dimensions, which is consistent with the previous reports [S4-S6] and could be exploited for detecting the incident wavelength. The images in the upper and lower part of Fig. S9(a) are higher-order holographic images. Meanwhile, though the image contents are the same for different illumination wavelengths due to the dispersion-less nature of the PB phase, there are some angular distortions to the designed holographic image: the rings and disks are no longer perfectly circular. Larger deviations from the 800 nm design wavelength will cause larger imaging distortions. This will introduce additional errors in identifying the chiral phase difference and thus the polarization state. Figures S9(e) to S9(h) show the chiral phase differences and Stokes parameters extracted from these distorted images at

650, 850 and 900 nm wavelength, and compare them with the corresponding results at 800 nm wavelength, supposing that the waveplate in Fig. 4(a) is a quarter-wave plate. In spite of the image distortions, the polarization state is extracted with relatively good accuracy, indicating broadband operation of the meta-hologram.
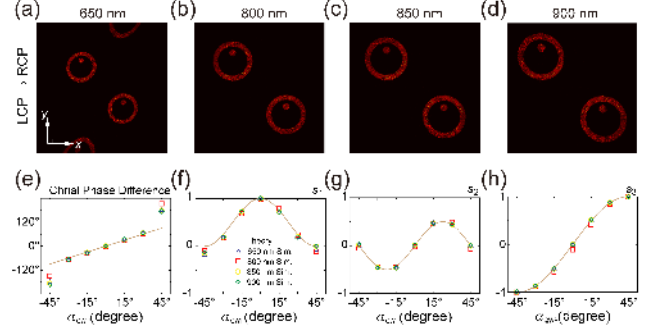

Fig. S9. Simulated wavelength-dependent holographic images and polarization extractions. (a-d) Simulated RCP holographic images generated under LCP illumination at 650, 800, 850 and 900 nm wavelength, respectively. (e-h) Theoretical and simulated extractions of chiral phase differences (e) and Stokes parameters s_1, s_2 and s_3 (f-h) when rotating the quarter-wave plate at the four selected wavelengths, respectively. Here, the simulations are carried out by supposing that the waveplate in Fig. 4(a) is a quarter-wave plate.
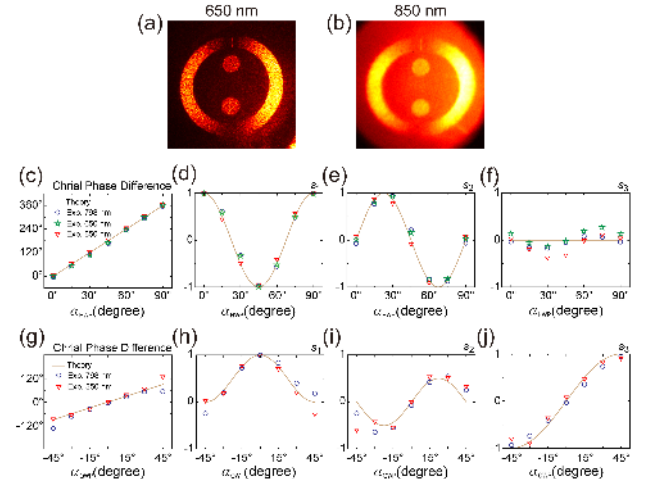

Fig. S10. Measured wavelength-dependent holographic images and polarization extractions. (a,b) Measured *x*-polarized component of the holographic images generated by *x*-polarized metasurface illumination at 650 and 850 nm wavelength, respectively. (c-f) Theoretical and experimental chiral phase differences (c) and Stokes parameters s_1, s_2 and s_3 (d-f) when rotating the half-wave plate of Fig. 4(a) at 650, 798, and 850 nm wavelength. (g-j) Theoretical and experimental chiral phase differences (g) and Stokes parameters s_1, s_2 and s_3 (h-j) when rotating the quarter-wave plate of Fig. 4(a) at wavelengths of 798 and 850 nm.

Figure S10 shows the measured *x*-polarized component of the holographic images under *x*-polarized illumination, and the measured chiral phase differences and Stokes parameters at 650,

798, and 850 nm wavelength, supposing the waveplate in Fig. 4(a) is a half-wave (quarter-wave) plate. It is seen that the measured results are in relatively good agreement with the theory. Since 850 nm is out of the working range of our camera, an IR viewer is placed before the camera. The larger errors measured at 850 nm may have resulted from the noise of the IR viewer.

Section 10: An improved design method for avoiding angular distortion

To avoid angular distortion of the ring and to increase the accuracy, an improved design is proposed by putting the same ring and disk pattern at the center of the holographic plane, as illustrated in Fig. S11. It is seen that even though the target and twin images overlap with each other, the operation of the final ring and disk patterns for LCP and RCP illuminations is not affected.
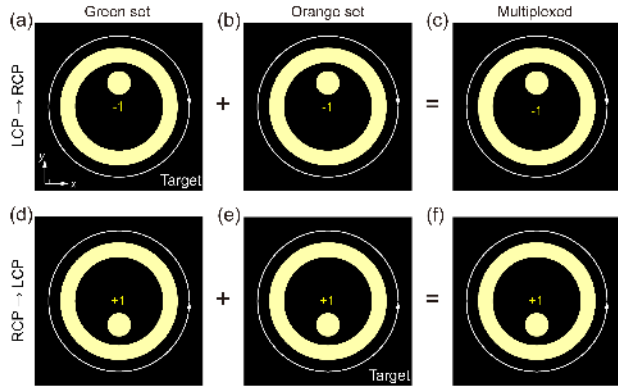

Fig. S11. Schematics of the image generation with the ring at the center of the holographic plane. (a, e) Schematics of the RCP and LCP holographic images of the green and orange resonator sets of the meta-hologram generated by LCP illumination and RCP illumination, respectively. (d, b) Schematics of the corresponding LCP and RCP twin images generated by the reversed circularly polarized illumination. (c, f) Schematics of the RCP and LCP holographic images of the multiplexed meta-hologram generated by LCP illumination and RCP illumination, respectively

The rings in this case will be perfectly circular for any illumination wavelength, despite angular distortions beyond the design wavelength, as illustrated by the simulated results in Figs. S12(a) to S12(c). However, it would be better to generate such holographic image with larger efficiency to reduce the influence from the zero-order output in real experiments. This can be done by using reflection-type or dielectric metasurfaces [S2,S6]. Figures S12(d) to S12(g) illustrate the corresponding extracted chiral phase differences and Stokes parameters at the design wavelength of 800 nm, supposing that the waveplate in Fig. 4(a) is a quarter-wave plate and that the cross-polarized efficiency of the structure is 80%. It is seen that the simulated results agree well with the theory, also for this modified hologram design.
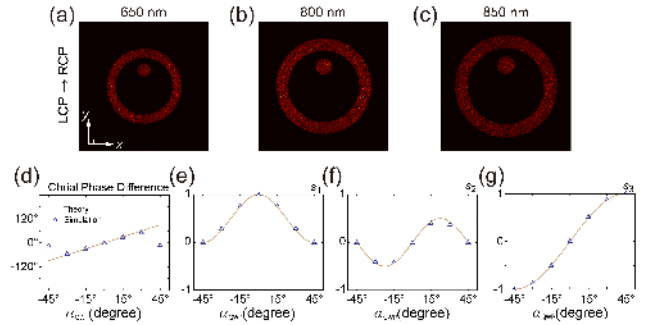

Fig. S12. Improved meta-hologram polarimetry with the ring at the center of the holographic plane. (a-c) Simulated RCP holographic images generated under LCP illumination at 650, 800, and 850 nm wavelength, respectively. (d-g) Theoretical and simulated extraction of chiral phase differences (d) and Stokes parameters s_1, s_2 and s_3 (e-g) when rotating the quarter-wave plate at 800 nm wavelength, respectively. Here, the extractions are carried out by supposing that the waveplate in Fig. 4(a) is a quarter-wave plate, and that the cross-polarized efficiency of the structure is 80%.

Section 11: Partial polarization measurements

Under partially polarized illumination, the polarized component will follow the description in the manuscript. However, the unpolarized component is different. Though it will also contribute to the holographic image, i.e. generate an RCP ring containing an upper disk and an LCP ring containing a lower disk, these cannot interfere with each other since they are incoherent. Thus, the unpolarized component actually contributes a DC distribution to the final holographic image.

To determine the polarization state of a partially polarized incident light beam, besides the Stokes parameters of the polarized component, it is also necessary to know the degree of the polarization p. In this case, the Eq. (3) becomes:

$$\left| \text{PD}_x(\theta) \right|^2 = p \left[\frac{1}{2} r_0^2 + \frac{1}{2} l_0^2 + l_0 r_0 \cos(2\theta - \Delta\varphi) \right] + \frac{1-p}{2} . \quad \textbf{(S2)}$$

The chiral phase difference $\Delta\varphi$ can still be extracted by Fourier transforming the intensity distribution along the ring. The DC distribution will have a negligible influence on the chiral phase difference measurement, since it mainly contributes to the 0th order in the Fourier domain.

For the chiral amplitude contrast $a = r_0/l_0$, the extraction becomes more complicated as it cannot be calculated solely from the intensities of the disks, which also contain the DC distribution from the un-polarized component. In this case, additional information from the intensity distribution along the ring is required. Neglecting the zero-order output noise and the background noise, one can extract potential solutions for r_0, l_0 and p by fitting the intensity distribution along the ring. There should be solutions for r_0 and l_0 with exchanged values. The correct solution can be identified by comparison of the integrated intensities from the upper and lower disks.

With the above extracted values, the degree of the polarization and the Stoke parameters of the polarized component can be calculated by using Eqs. (4) to (6).

Reference

S1. R. W. Gerchberg, W. O. Saxton, "A Practical Algorithm for the determination of phase from image and diffraction plane pictures," OPTIK **35**, 237–246 (1971).

S2. D. Wen, F. Yue, G. Li, G. Zheng, K. Chan, S. Chen, M. Chen, K. F. Li, P. W. H. Wong, K. W. Cheah, E. Y. B. Pun, S. Zhang, X. Chen, "Helicity multiplexed broadband metasurface holograms," Nat. Commun. **6**, 8241 (2015).

S3. F. Shen, A. Wang, "Fast-Fourier-transform based numerical integration method for the Reyleigh-Sommerfeld diffraction formula," Appl. Opt. **45**, 1102-1110 (2006).

S4. X. Zhang, J. Jin, Y. Wang, M. Pu, X. Li, Z. Zhao, P. Gao, C. Wang, X. Luo, "Metasurface-based broadband hologram with high tolerance to fabrication errors," Sci. Rep. **6**, 19856 (2016).

S5. X. Li, L. Chen, Y. Li, X. Zhang, M. Pu, Z. Zhao, X. Ma, Y. Wang, M. Hong, X. Luo, "Multicolor 3D meta-holography by broadband plasmonic modulation," Sci. Adv. **2**, e1601102 (2016).

S6. M. Khorasaninejad, A. Ambrosio, P. Kanhaiya, F. Capasso, "Broadband and chiral binary dielectric metasurface holograms," Sci. Adv. **2**, e1501258 (2016).